Differentiated strain-control of localized magnetic modes in antidot arrays

N. Challab[1],† D. Faurie[1],† M. Haboussi[1],† A. O. Adeyeye[2,3],† and F. Zighem[1†]

†[1]*LSPM-CNRS UPR3407, Université Sorbonne Paris Nord, 93430 Villetaneuse, France*

‡[2]*Information Storage Materials Laboratory Department of Electrical and Computer Engineering National University of Singapore 117576 Singapore, Singapore*

¶[3]*Department of Physics, Durham University, South Road, Durham DH1 3LE, United Kingdom*

E-mail:

Abstract

The control of localized magnetic modes has been obtained in $Ni_{60}Fe_{40}$ square lattice (600 nm) antidot arrays. This has been performed by tailoring the magnetoelastic field at the scale of the antidot primitive cell. The corresponding heterogeneous strain field distributions have been generated by a PZT substrate and enhanced by the incorporation of a supporting compliant layer. It has been highlighted by a differentiated variation of magnetic energy, directly due to the local magnetoelastic field felt by each magnetic mode, probed by ferromagnetic resonance spectroscopy. A modeling, involving micromagnetic simulations (to locate the magnetic modes), full-field simulations (to evaluate the strain field distributions) and an analytical model generally dedicated to continuous film that we have extended to those magnetic modes, shows a well agreement with the experimental data. This approach is very promising to develop multi-channel systems with simultaneous and differentiated controlled frequencies in magnetic devices.

Introduction

Nanoscale magnetic systems have many applications, particularly in the field of data storage, transmission and processing. Nowadays, several avenues are being explored to exploit the unique properties of these materials. These include the exploitation of magnetic skyrmions [1,2], magnetic memories [3,4], heat assisted magnetic recording [5] or magnonic systems [6–8]. One of the challenges is to control the magnetic properties in a reversible way with low energy consumption, especially their dynamic properties for high-frequency systems [9,10]. This can be achieved by using electric or elastic-strain fields (magnetoelastic effect) instead of using a magnetic field [11,12]. These effects have been widely reported in the literature, typically for continuous thin films on ferroelectric substrates [13–15]. However, the magnetoelastic field obtained for continuous films is generally homogeneous, which makes difficult to spatially control differently the spin wave energies [16].

A degree of freedom can be achieved by fabricating arrays of magnetic nanostructures. In this case, the different translational invariance breaks give rise to spatially localized spin wave modes which ultimately have a different magnetic behavior, this is particularly true for magnonic crystals [17–19]. Indeed, magnonic based devices can lead to inventive and low power applications such as microwave resonators, filters, spin wave logic devices for information transport [20–22]. However, although spin wave energies (magnonic bands) are easily controllable by applying a magnetic field, it is difficult to individually tailor each mode [23]. One can imagine controlling separately these spatially localized spin wave modes by applying local magnetic fields [24]. While it is not straightforward to control a magnetic field at the scale of mode localization, it is possible to take advantage of the geometrical (and thus mechanical [25]) heterogeneity to obtain a position-dependent magnetoelastic field. To achieve this goal, antidot-type systems are well suited because an external macro-strain will be periodically distributed in a non-homogeneous manner, as well as the localization of magnetic modes [26–29]. This is all the more the case as a supporting layer is compliant since it should accommodate the strain heterogeneities that are known to take place in holed structures [30].

Furthermore, the differentiated sensitivity to the strain field of the magnetic modes may depend on the orientation of the system with respect to the external strain.

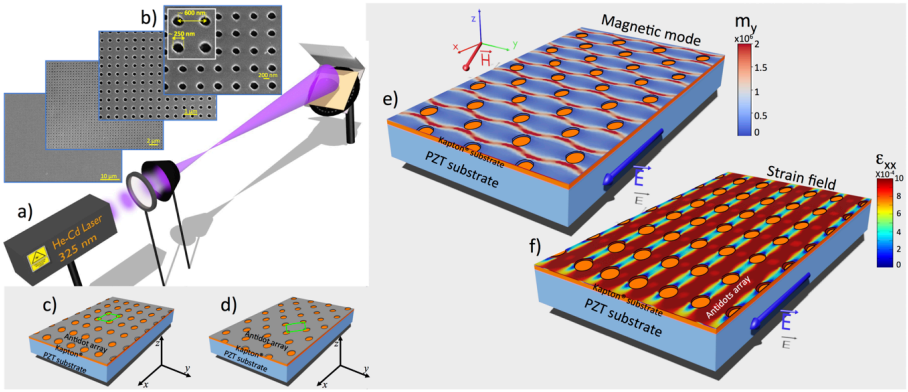

Figure 1: a) Schematic of the interference lithography technique showing the Lloyd's mirror interfometer. b) Scanning electron microscopy images (with different enlargement) of a $Ni_{60}Fe_{40}$ antidot array, the periodicity (600 nm with a nanohole diameter of 200 nm) of the array is indicated in the image with the largest zoom. c-d) Sketch of the two studied systems (magnetic antidots/Kapton®/PZT substrate); the array is either aligned along x-axis of the PZT substrate (Square Array -SA- system in c) or it makes a 45° angle with respect to the x-axis (Centered Square Array -CSA- system) in d). e-f) Illustration of magnetic mode and strain field distributions mapping . e) The map corresponds to the profile (m_y component) of one of the studied magnetic mode obtained with a static magnetic $\vec{H}$ applied along x in the CSA system. A red color in the mapping means a high amplitude spin precession while a blue color means zero amplitude. f) Example showing a mapping of calculated strain field distribution (ε_{xx} component here) in the array of antidots when an electric field is applied to the PZT substrate in the SA system.

In this paper, we propose a concept using two levers to locally control the magnetic modes: i) the mechanical contrast between the antidots and the support layer and ii) the geometrical characteristics of the system. This approach is still unexploited in the literature. It has been validated by the study of strain fields and magnetic mode energies in $Ni_{60}Fe_{40}$ antidot arrays. In order to optimize strain heterogeneities, the antidots have been first fabricated on a supporting compliant polyimide layer and then cemented onto a ferroelectric substrate generating macroscopic strain (figure 1)[31]. The correspondence between the localization of mechanical and magnetic quantities was analyzed by numerical modeling in order

to predict the differentiated change in spin wave mode frequencies as a function of the external strain (figures 1e-f)). Magnetic antidot arrays present both magnetic heterogeneities (through localized magnetic modes due to in-plane invariance break) and mechanical ones (due to the presence of free surfaces and to the mechanical contrast between Kapton® and $Ni_{60}Fe_{40}$ material). We have used double numerical modeling to spatially locate the different magnetic modes with their energies (1-e)) and to quantitatively determine the in-plane strain distributions (1-f)) in the antidot arrays. Then, the local magneto-mechanical coupling can be estimated using a "classical" magnetoelastic formalism. The magnetic problem was solved by performing 3D micromagnetic simulations thanks to OOMMF package[32] and the mechanical one was solved by using COMSOL Multiphyics® software[33]. The experiments have been performed by *in situ* ferromagnetic resonance (FMR) spectroscopy. Analysis of the data shows that the different magnetic modes can have their frequency modified, the shift being strongly dependent on their localization (difference of several tens of %). Furthermore, the rotation of the system as referred to the external strains (and magnetic field) causes a strong modification of this dependence since it changes the localization of the magnetic modes and the mechanical strains. In the remainder of this paper, we first present the experimental setup used and the methodology adopted to study the phenomena of interest, then the magnetic behavior of the studied system is reported including the numerical comparison. Then, the strain localization in the corresponding structure is studied to finally adjust a magnetoelastic model to reproduce the magnetic behavior of the localized modes. We beleive that this study provides additional leverage for the manipulation and control of magnetic modes in future applications in spintronics, straintronics and flexible magnonics. The heterogeneities due to nanostructuring are seen in a global sense since they concern the mechanical fields and the localization of the magnetic modes. This type of study will probably become more widespread as the miniaturization of components and the increasingly complex nanoarchitectures will generate this kind of complex coupled phenomena.

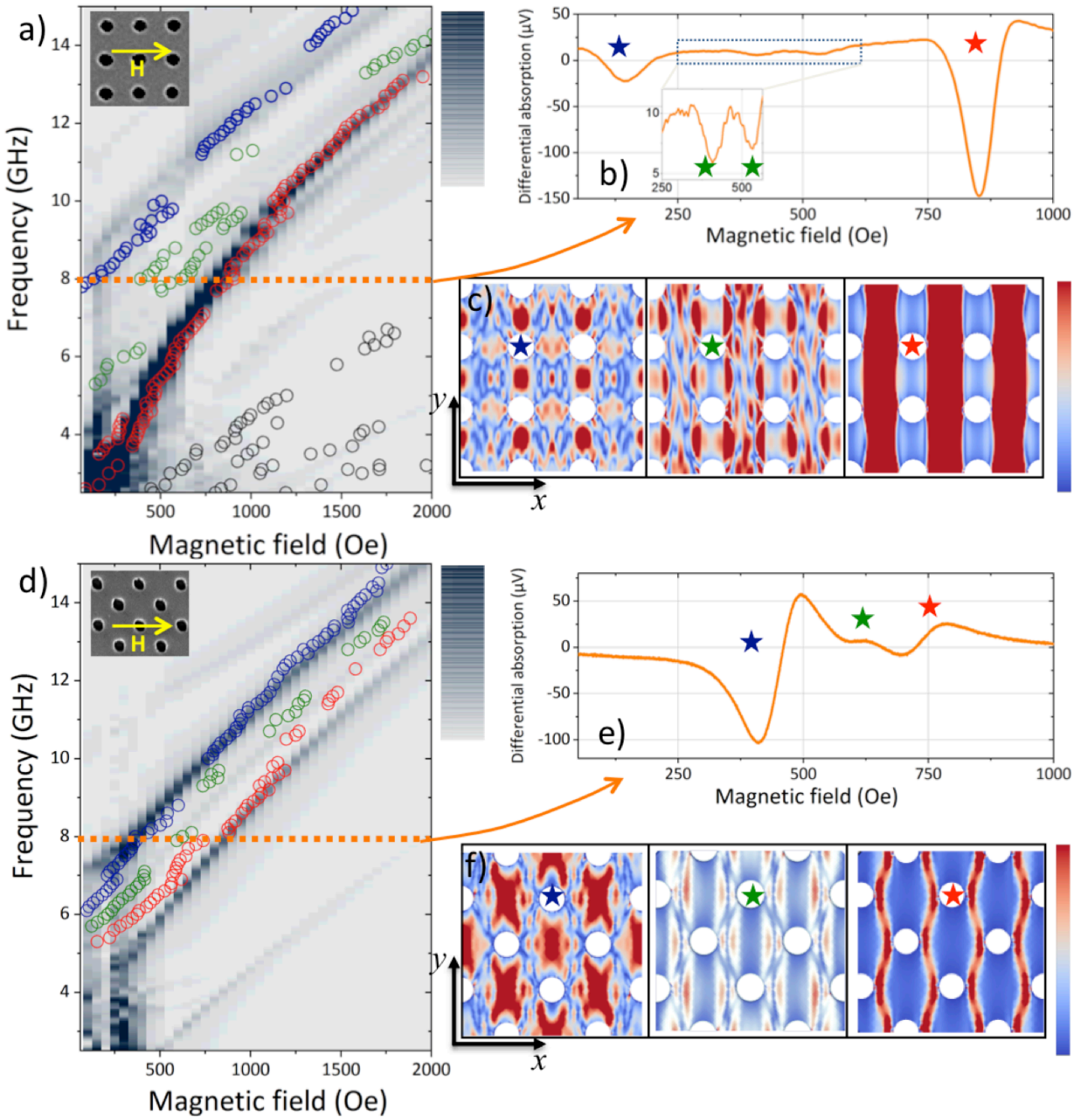

Figure 2: Experimental and numerical results obtained with a magnetic field applied along x-axis in absence of electric field for the two studied systems. a-c) SA system and d-f): CSA system. a),d)) Frequency as function of the applied magnetic field. The colors correspond to the relative power spectrum density obtained by micromagnetic simulations while the open symbols are experimental data. b),e) Typical experimental spectrum recorded at 8 GHz, the stars are used to identify the different peaks. c),f) Spin precession amplitudes at $H = 750$ Oe (applied along $x-$axis) obtained by micromagnetic simulations (spatial Fourier transform) showing the localization of the modes identified in the FMR spectra. The colors encode m_y component, the red part reflects a high precession amplitude while the blue one means zero precession amplitude. The stars inside the images correlate the mode profiles with positions in the FMR spectra (a) and d)).

Localized magnetic modes in absence of elastic strains

In order to enhance the mechanical contrast between the magnetic antidots and the PZT substrate which leads to a significant increase of the voltage-induced strain heterogeneities, we inserted a polymer layer between the two media. The antidot arrays have been first fabricated on top of a polymer layer (127.5 µm) and then we have cemented the polymer/antidot systems on a ferroelectric substrate. We have used the Interference Lithography (IL) technique (figure 1-a)) to fabricate 2D square antidot arrays on top of a polymer layer (see Methods). The obtained structure consists of 20 nm thick $Ni_{60}Fe_{40}$ antidot arrays of diameter 250 nm and the centre-to-centre spacing between nearest nano-holes is 600 nm, as shown in figures 1-b). Finally, the Kapton®/antidots system was cemented on a PZT substrate[34]. Depending on the angle between the antidots array and the main axis of the ferroelectric substrate, two configurations have been studied. The first one has been obtained by gluing the antidot array along the main axis ($x-$axis) of the ferroelectric substrate while the second one has been obtained by gluing the antidot array at 45° with respect to $x-$axis; a sketch of each configuration is presented in figures 1-c) and 1-d). Thereafter, the first configuration will be called Square Array (SA) system and the second one will be called Centered Square Array (CSA) system. This two extreme configurations have been defined in order to obtain significantly different strain heterogeneity maps, as described in the following sections. Finally, for comparison, a reference 20 nm thick $Ni_{60}Fe_{40}$ continuous film has been also fabricated and studied.

FMR response of the antidot arrays was measured at room temperature by sweeping the applied magnetic field in the range 0-2500 Oe at different fixed frequencies (from 0.1 to 15 GHz). Moreover, a lock-in amplifier locked to the ac field frequency (~ 5 Oe at 160 Hz) was employed to detect the FMR absorption signal[35]. In figure 2-b), a typical FMR spectrum recorded at 8 GHz from the SA system is presented. A multi-modal response (see stars) is clearly observed as compared to the reference continuous film which presents a unique mode (not shown here). In this spectrum, we observe two prominent peaks and two weaker ones

(highlighted by a zoom-in). This difference in intensity between peaks suggests that they originate from fundamental resonance of different spatial regions of the antidot system[36]. We have plotted the whole experimental frequency peak positions in figure 2-a) that are represented by open symbols. At low frequencies (below 6 GHz), some modes (open black symbols) with very weak intensities are present at high magnetic field that are generally due to a dynamic precession at the edge of the nano-holes[37,38]. At higher frequencies (above 7 GHz), the two major peaks (blue and red stars in figure 2-b)) are easily detectable in almost the entire range of frequencies (7-14 GHz) while the weaker ones were only intermittently detectable, certainly due to their weaker initial intensity. Micromagnetic simulations giving the frequency positions and relative intensities are also presented in figure 2-a) using a relative color mapping from 0 to 1. One can note the good agreement between experimental and simulated data at a high frequency (above 7 GHz) while small discrepancies appear for the modes represented with black open symbols. However, these discrepancies are not surprising since these modes are certainly very localized (edge modes) and are known to be strongly sensitive to small defects[39,40] (roughness of the nano-holes, small variation of the nano-holes diameter or in the composition just near the nano-holes,...) that are difficult to simulate precisely.

Similar results have been obtained in the CSA system. A typical spectrum recorded at 8 GHz is presented in figure 2-e) showing again two pronounced peaks (red and blue stars) and one weaker peak (green star). We note that the peaks are closer in term of energy. Indeed, the difference between the two pronounced modes is $\sim$ 300 Oe for the CSA system (see figure 2-e)) and $\sim$ 800 Oe for the SA system (see figure 2-b)). This shrinking of the FMR spectra is confirmed by the whole frequency dependence (see figure 2-d)) where the experimental data are represented by open symbols. In addition, we also note a permutation in the relative intensities between the higher frequency (blue star) peak and the lower frequency (red star) one as compared to the SA system. For instance, in figures 2-b) and 2-e), the intensity ratio between the higher frequency peak and the lower frequency one is $\frac{I^{blue}}{I^{red}} \simeq 0.18$ for the SA

system whereas it is $\frac{I^{red}}{I^{blue}} \simeq 0.19$ for the CSA system. In order to precisely determine the microscopic origin of each peak of both systems (SA and CSA), we have used spatial Fourier transform imaging. The main results are presented in figures 2-c) and 2-f) where mappings of the spin precession calculated for a magnetic field of 750 Oe are presented. The colors encode m_y component, the red part reflects a high spin precession amplitude while the blue one means zero spin precession amplitude. For both systems, all the modes correspond to spin excitation that are localized in more or less extended regions.

Concerning the SA system, we have the confirmation that the higher peak (red star) in intensity corresponds to a mode localized in a broader region than the other ones. This mode corresponds to a "spin wave" that extends through the antidot array and can be considered as a backward volume type mode[38,41]. Indeed, in first approximation, an effective quantized wave-vector can be associated to this mode along x-axis, i.e. in the direction of the applied magnetic field $\vec{H}$ (and to the static magnetization that is almost homogeneous, at least above 500 Oe)[41]. On the other hand, the higher frequency mode is related to the spin excitation located between neighboring nano-holes and can be considered as a Damon-Eshbach-type mode[41,42]. Indeed, in this case, an effective quantized wave-vector can be associated to this mode along y-axis, i.e. in the direction perpendicular to the applied magnetic field[41]. Concerning the CSA system, it is interesting to note that higher and lower frequency modes possess profiles quite resembling those obtained for the SA system and can be explained if one remembers that the difference between SA and CSA in the subsection is only a 45° rotation of the applied magnetic field. Furthermore, one can note that the higher frequency mode (blue star) profile is now more extended than the lowest frequency one, explaining the intensity inversion in the FMR spectra. Finally, it is worth noting that the profile evolutions displayed for SA and CSA systems show that the lower frequency mode profile is sharpened along x (and presents an oscillatory profile along y) while the higher frequency one is broadened along y. The effective wave-vector associated to these mode profiles is thus enhanced for the lower frequency mode (red stars) when switching from SA to CSA system

while it is reduced for the higher frequency mode (blue stars). Consequently these evolutions yield an increase of the lower frequency mode energy and a decrease of the higher frequency mode energy because of exchange contribution and can explain the closeness of the FMR peak modes in the CSA system as compared to the SA one.

After this magnetic mode identifications, it is important to link it with the strain distributions in the antidot systems induced by the application of an electrical voltage inside the PZT substrate. This evaluation has been performed thanks to full-field modeling and is presented in the next subsection.

Heterogeneous strain fields

As discussed in the introduction, the voltage induced strain field distribution is heterogeneous in our antidot arrays due to the presence of free surfaces and is enhanced by the mechanical contrast between Kapton® and $Ni_{60}Fe_{40}$ material as we will see in this subsection. We have first characterized the strains in the continuous film that are totally transmitted between the PZT substrate and the top surface of continuous film by using the Digital Image Correlation technique from optical tracking of the mottled surface; more details about this technique can be found in ref.[35]. The deduced mean in-plane strain components (ε_{xx}^{sub} and ε_{yy}^{sub}) as a function of the applied voltage (by step at around 2 V) are presented in figure 3-b) (blue and red circles). One can note that ε_{xx}^{sub} is found to be positive and ε_{yy}^{sub} is found to be negative in the range (0-100 V) and that they vary almost linearly. The maximum values at 100 V are found to be $\sim 0.1 \times 10^{-2}$ for ε_{xx}^{sub} and $\sim -0.05 \times 10^{-2}$ for ε_{yy}^{sub}. Moreover, non-linear and hysteretic behaviors for ε_{xx}^{sub} and ε_{yy}^{sub} can be observed if the voltage is swept backward from 100V to 0V (not shown here) due to the intrinsic properties of the PZT substrate[34]. DIC measurements performed in the antidot systems show similar results. Indeed, the resolution of our DIC technique was not sufficient to depict local strain heterogeneities at the surface of the antidot systems. This is the reason why we have decided to perform numerical simulations

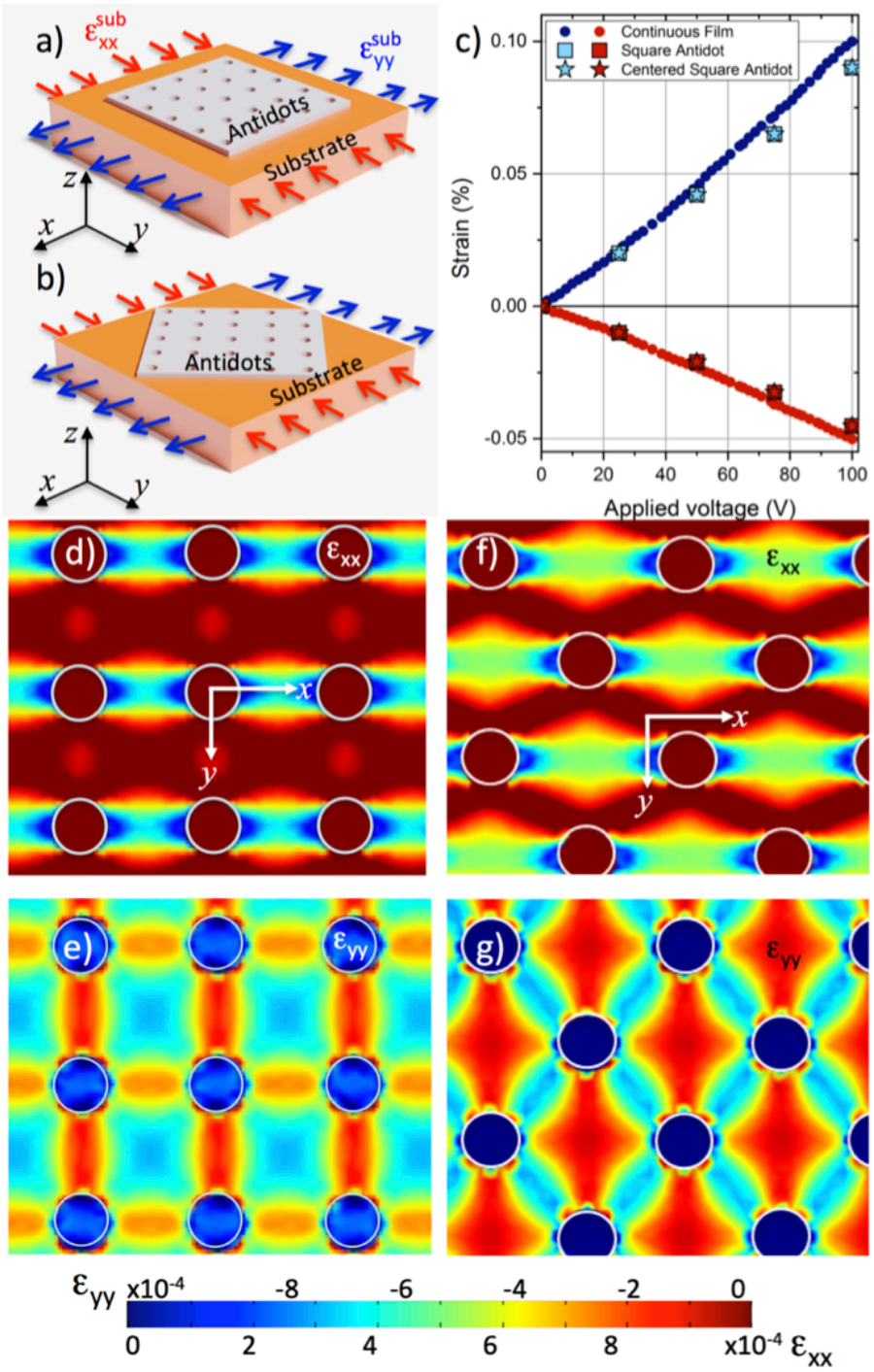

Figure 3: a-b) Sketches of the simulated systems. The imposed strains to the Kapton® layer $\varepsilon_{xx}^{\text{sub}}$ and $\varepsilon_{yy}^{\text{sub}}$ are the ones determined from digital image correlation measurements in the continuous film system. c) Mean values of in-plane strain components (ε_{xx} and ε_{yy}) measured in the film system and calculated in the SA and CSA systems. d-g) 2D mapping of the in-plane strains (ε_{xx} and ε_{yy}) in the SA (d-f) and CSA (e-g) systems. These maps have been obtained with imposed strains corresponding to a voltage of 100V.

using COMSOL Multiphysics® software[33].

Figures 3-a) and 3-b) show a schematic presentation of the simulated systems: SA (a) and CSA (b). The strain values imposed on the Kapton® layer are those derived from DIC measurements. We have applied four pairs of strains to the Kapton® layer corresponding to applied voltage of 25, 50, 75 and 100 V. In the simulations, we assumed isotropic mechanical properties for both Kapton® ($Y_{\text{Kapton}} = 4$ GPa for the Young's modulus and $\nu_{\text{Kapton}} = 0.3$ for the Poisson's ratio) and $Ni_{60}Fe_{40}$ materials ($Y_{Ni_{60}Fe_{40}} = 205$ GPa and $\nu_{Ni_{60}Fe_{40}} = 0.3$ obtained by a homogenization method from the bulk material[43]). As experimentally observed by DIC, the mean in-plane strains calculated in the antidot arrays are close to the one of the continuous film. Indeed, in figure 3-b), we have reported the calculated mean in-plane strains inside the antidot systems (square symbols correspond to the SA system while stars correspond to the CSA system). In addition, we have also estimated the mean strains for a continuous film of the same xy dimensions, one can note that the calculated mean strains are also very close to the one imposed by the Kapton® layer.

However, while the strain distributions are homogeneous in the continuous film, they are very heterogeneous in the antidot systems. For instance, figures 3-d-e) and 3-f-g) show the calculated strain distributions at the top surface of the SA and CSA systems under 100 V. We clearly observe local strain variations of several tens of percent. Note that the scale color of ε_{xx} is positive while it is negative for ε_{yy}. Interestingly, one can see that to some extent, the strain fields mimic the magnetic profiles whatever the direction of the imposed principal strain and the static applied magnetic field, respectively. Indeed, for instance, we retrieve the oscillating behavior of the low frequency mode in the CSA system through an oscillating ε_{xx} strain field and the more localized profile of the high frequency mode between nano-holes in the CSA system through the ε_{yy} strain field . Moreover, as for the magnetic mode profiles evolution between SA and CSA system, we found that the ε_{xx} strain field is sharpened while the ε_{yy} strain field is broadened. These behaviors are certainly due to the symmetry of the antidot array which imposes in a certain sense these magnetic and mechanical "confinements"

of the magnetic modes and of the strain fields, respectively. Afterward, we will take advantage of this symmetry to study the influence of these local strains on the magnetic mode energies because this will impose heterogeneous magnetoelastic fields that *in fine* will mimic the strain distributions.

Finally, as written before, this heterogeneity is *a priori* enhanced by greater mechanical contrast between the antidot and the Kapton® strained by the PZT substrate. In this highly mechanically contrasted system ($Y_{Ni_{60}Fe_{40}}$ = 205 GPa, Y_{Kapton} = 4 GPa), we obtain a range of strains that can vary over two orders of magnitude. However, we wanted to show that this heterogeneity is indeed much lower for the systems with lower mechanical contrast. For this purpose, simulations varying the Young's modulus of the supporting layer were carried out. The results are shown in figure 4 representing the 2D strain field for a Kapton® layer and a 1D profile for substrates of various Young moduli, for ε_{xx} (figure 4-a)) and ε_{yy} (figure 4-b)). It is clearly seen that the amplitude of the strain variation decreases as the Young's modulus increases, *i.e.* as the mechanical contrast decreases. In this case, for an applied voltage of 100 V, the strain state in the substrate is given by ε_{xx} = 0.1% and ε_{yy} = -0.05%. Even if the homogeneous strain state is never reached because of the nano-holes, it is still approached when the Young's modulus of the substrate is close to that of the antidot, as it would be the case for a rigid substrate (around 200 GPa). And, on the contrary, when the supporting layer is very compliant like Kapton®, the strains can be much higher or much lower than those imposed on the substrate. This shows that the high substrate compliance is a determining factor in the search for highly contrasted local magnetoelastic fields over the entire surface of the antidot, thus allowing very diverse variations in localized mode frequencies to be obtained by controlling strain heterogeneities in antidot systems. In addition, it should be noted here that the transmission of strains (in the average sense) is optimized by the fact that the Kapton® substrate is very thick compared to the antidots (about 5000 times)

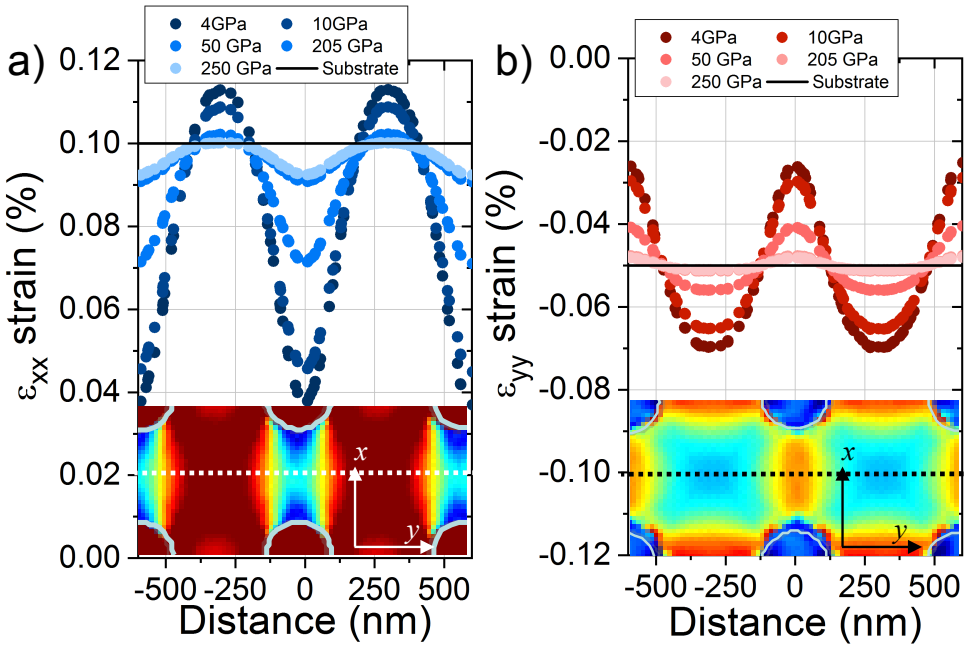

Figure 4: Evolution of the strains heterogeneities as function of the mechanical contrast between the antidots and the substrate: a-b) Profiles of in-plane strains (ε_{xx} (a), ε_{yy} (b)) for different values of the Young's modulus substrate, from 4 GPa to 250 GPa. The cut-lines are indicated by dashed lines in the maps. The in-plane strains of the substrate have been fixed at $\varepsilon_{xx} = 1 \times 10^{-3}$ and $\varepsilon_{yy} = -0.5 \times 10^{-3}$.

Strain control of the localized magnetic modes

As discussed before, mapping of the elastic strain field and of the magnetic modes has highlighted some similarities that will be very helpful in this subsection. Indeed, due to obvious square-symmetry reasons, the magnetic mode profiles remain unchanged if a transverse in-plane magnetic field is applied (i. e. along y-axis), except that their localization pattern undergoes a 90° rotation[38]. On the other hand, the elastic strain field remains unchanged because it is not sensitive to this applied magnetic field. Thus, a given magnetic mode can be studied under two distinct strain states geometry by successively applying the magnetic field along x and y.

Figures 5-a-c) present typical FMR spectra at zero applied voltage (blue lines) and at 100 V (red lines) from the reference continuous film, the SA and the CSA systems, respectively. These spectra have been recorded in similar conditions, i.e. at 8 GHz and by applying a

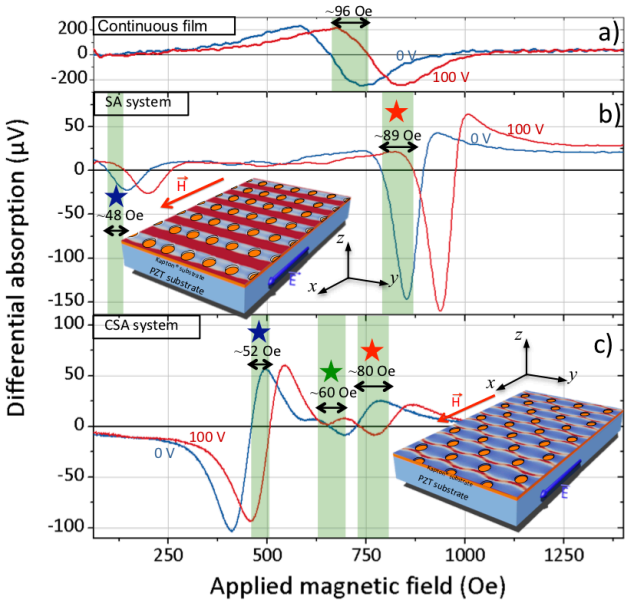

Figure 5: Typical 8GHz-FMR spectrum obtained at 0V (blue lines) and at 100 V (red lines) for the continuous film (a), the SA system (b) and the CSA one with a magnetic field applied along x. Sketches presenting the SA and CSA system are also depicted to see the coordinates; the mapping correspond to the low frequency mode in both cases (red stars in the spectra).

static magnetic field along x. All the spectra present a shift of all the absorption peaks. As previously mentioned, the continuous film presents a unique peak which corresponds to the uniform precession mode. We observe an up-shift of its resonance field ($\sim$ 96 Oe at 100 V) which means that the magnetostriction coefficient is positive. By applying the methodology presented in ref.[44], one can quantitatively determine the magnetostriction coefficient λ. Thus, the resonance field shift $\delta H_{res} = H_{res}(0) - H_{res}(\mathrm{V})$ can be well fitted using the following relation for an applied magnetic field along x[34]:

$$H_{res} = \sqrt{\left(2\pi M_s - \frac{3\lambda}{M_s}\sigma_{yy}^{sub}(\mathrm{V})\right)^2 + \left(\frac{2\pi f}{\gamma}\right)^2} - 2\pi M_s - \frac{3\lambda}{M_s}\left(2\sigma_{xx}^{sub}(\mathrm{V}) - \sigma_{yy}^{sub}(\mathrm{V})\right) \quad (1)$$

where $\sigma_{xx}^{sub}(\mathrm{V})$ and $\sigma_{yy}^{sub}(\mathrm{V})$ are the in-plane principal stress tensor components of the film calculated from the measured in-plane strains $\varepsilon_{xx}^{sub}(\mathrm{V})$ and $\varepsilon_{yy}^{sub}(\mathrm{V})$ and the Hooke's law[45]. Under these conditions, the magnetostriction coefficient is found to be $\lambda = 12 \times 10^{-6}$. This

value has been obtained by fitting the whole δH_{res} voltage as presented in figure 6 where the black symbols are experimental data and the black line is the calculated fit. In the following, we assumed that λ is the same for $Ni_{60}Fe_{40}$ antidots which have been elaborated at same time.

Concerning the SA and CSA spectra presented in figures 5-b) and c), we clearly observe that all the modes also present an up-shift which is however lower in magnitude than that in the continuous film. In addition, the shifts are not similar for all peaks in a specific system. For instance, in the SA system, the high frequency mode (blue star) presents a shift of $\sim$ 50 Oe while it is around 90 Oe for the low frequency one (blue star). A similar tendency is observed in the CSA system, the high frequency mode (blue star) presents a $\sim$ 50 Oe shift while it is around 80 Oe for the low frequency one. The weaker mode in intensity (green star) presents an intermediate shift of around 60 Oe. Thus, we have conducted FMR measurements in the range 0-100 V with a step of 1V at 8 GHz. Figures 6-a) and b) present the resonance field shifts of the different modes as a function of the applied voltage. It should be noted that, for the SA system, we do not plot the results of the two satellite peaks (green stars in figure 2) because of their weak intensities giving too dispersed results as a function of the applied voltage. This can be seen in the δH_{res} voltage dependence of the CSA modes: the higher the initial intensity of the modes, the lesser noise is generated by the voltage dependence. We have the confirmation that lower field shifts are obtained for the antidot systems as compared to the continuous film. Interestingly, the FMR shift is very different for the high frequency and low frequency modes in both antidot systems. We are convinced that this is due to their spatial localization and consequently to the local magnetoelastic field that is strongly heterogeneous as discussed in the precedent subsection. To confirm this assumption, we have taken advantage of the square-symmetry to perform measurements with an applied magnetic field along y. All other things being equal, only the magnetic modes have their localization rotated by 90°[38], notwithstanding the quality of the arrays that we have tested by FMR. Indeed, at zero applied voltage, the frequency dependencies

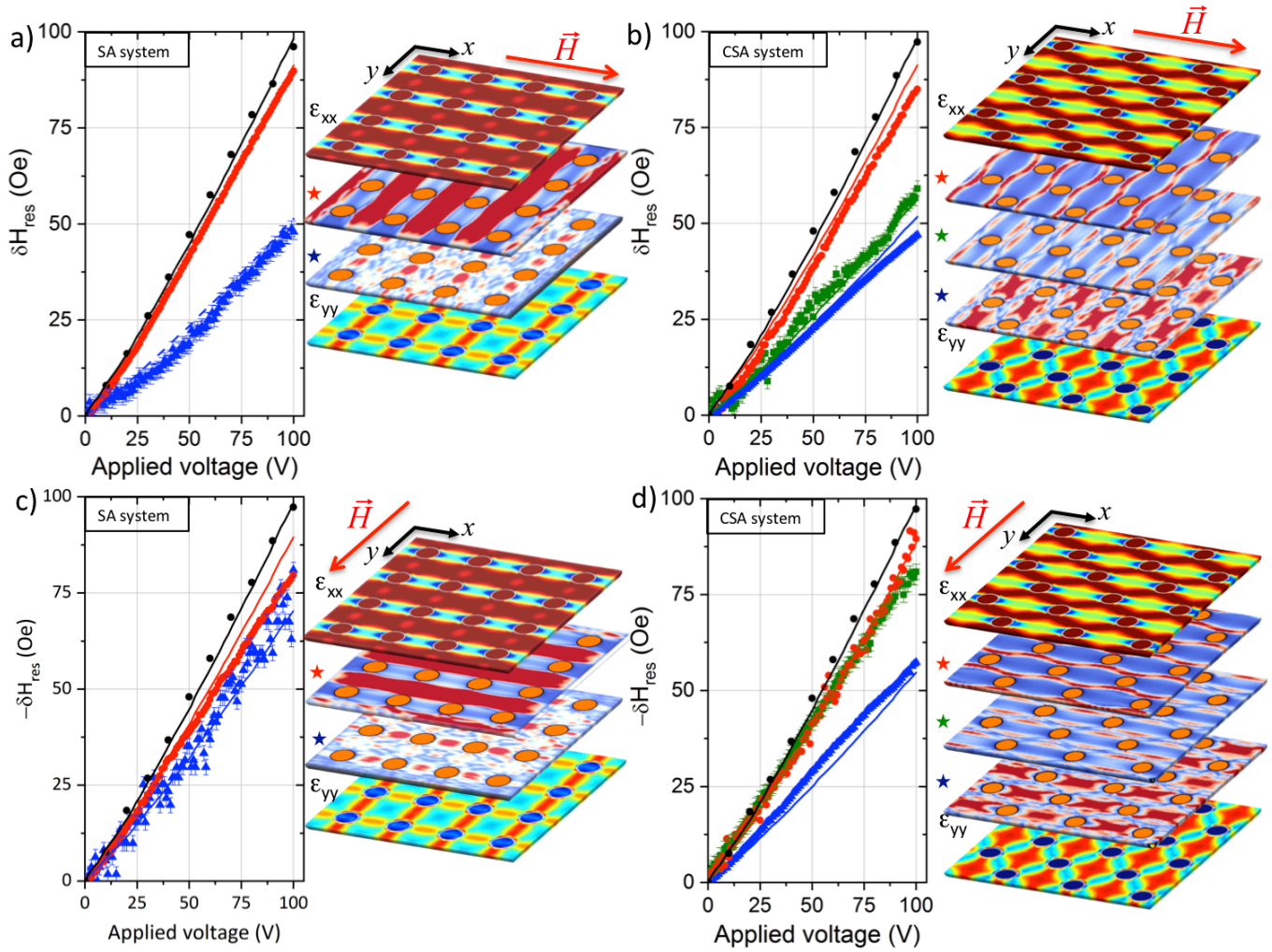

Figure 6: Resonance field shift as function of the applied voltage for the two systems with a magnetic field applied along (a-b) and perpendicular (c-d) to the PZT substrate. The different magnetic mode profiles are represented by maps where the colors encode either m_y (in a-b) or m_x (in c-d) components. We also present the maps of the in-plane strains (ε_{xx} and ε_{yy}) calculated in the antidot array systems. The colored symbols correspond experimental data while the color lines are calculated using the different α_{xx} and α_{yy} (see table 1). The black lines and symbols (full and dotted) correspond to experimental data and simulated line for the continuous film .

as a function of an applied magnetic field obtained at 0 and 90° are very similar in both systems (not shown here). This can be seen in the mapping of the strain field and of the the magnetic mode profiles presented in figures 6-a-d). In each figure, we have plotted the ε_{xx} and ε_{yy} strain fields as well as the profile of each studied magnetic modes. We clearly see that a specific mode (the high frequency mode of the SA system for instance) sees its profile rotate by 90° while the strain fields remain unchanged. The corresponding δH_{res} voltage dependencies are presented in figures 6-c) and d) for the SA and CSA systems, respectively. To more directly compare the results, we have plotted $-\delta H_{res}$ values.

Table 1: Strain transmission factors α_{xx} and α_{yy} for the different modes and configurations , i. e. $\vec{H}$ along or perpendicular to the main axis of the PZT substrate (along x or y).

Magnetic mode	$\vec{H} \parallel \vec{x}$		$\vec{H} \parallel \vec{y}$	
	α_{xx}	α_{yy}	α_{xx}	α_{yy}
	Continuous film			
Uniform Mode	100	100	100	100
	Square Array			
High Frequency Mode ★	0.67	0.55	0.92	0.43
Low Frequency Mode ★	0.79	1.03	0.94	0.92
	Centered Square Array			
High Frequency Mode ★	0.59	0.47	1.05	0.85
Satellite Mode ★	0.56	0.72	1.01	0.69
Low Frequency Mode ★	0.78	1.01	0.66	0.54

For the SA system, the low frequency mode (red star) is only slightly affected by this rotation (δH_{res} evolves from $\sim$ 90 Oe to $\sim$ 80 Oe at 100 V) while the high frequency one (blue star) is more seriously affected (δH_{res} evolves from $\sim$ 50 Oe to $\sim$ 85 Oe at 100 V). This also applies to the CSA system, we clearly see that three studied modes are differently affected. Indeed, the low frequency mode then the high frequency one and finally the "satellite" mode are increasingly affected by this rotation. Indeed, the δH_{res} amplitude at 100 V increases by $\sim$ 5, $\sim$ 10 and $\sim$ 25 Oe, respectively. So, we have an evidence that the differentiated

evolution of these modes depends on the local strain field experienced by each mode. Thus, from the results obtained in the two previous subsections, we extracted the local strain field by making a mask for each magnetic mode which we stick on the elastic strain distribution maps to extract mean values for $\langle \varepsilon_{xx}^{mode} \rangle$ and $\langle \varepsilon_{yy}^{mode} \rangle$. Then, one can define two factors that express the strain localization (α_{xx} and α_{yy})[30]:

$$\alpha_{xx} = \frac{\langle \varepsilon_{xx}^{mode} \rangle}{\langle \varepsilon_{xx}^{sub} \rangle} \qquad \text{and} \qquad \alpha_{yy} = \frac{\langle \varepsilon_{yy}^{mode} \rangle}{\langle \varepsilon_{yy}^{sub} \rangle} \tag{2}$$

The different extracted values are reported in table 1 for each mode. One can note good correlation between α_{xx} and α_{yy} values and the FMR peak shift of each corresponding mode. For instance, the α_{xx} and α_{yy} values of the low frequency mode are bigger in the four studied situations in comparison to the low frequency mode values which effectively presents higher δH_{res} variations. Those values also corroborate the wide δH_{res} variations of magnetic modes when applying the magnetic field at 0° and 90°. It is for instance the case for the high frequency mode in the SA system whose maximum values of δH_{res} at 100 V increase from $\sim$ 50 Oe to $\sim$ 85 Oe while the $(\alpha_{xx}; \alpha_{yy})$ evolves from $(67; 55)$ to $(92; 43)$ and for the satellite magnetic mode (green) of the CSA system which δH_{res} values at 100 V evolves from $\sim$ 55 Oe to $\sim$ 80 Oe while the $(\alpha_{xx}; \alpha_{yy})$ evolves from $(56; 72)$ to $(101; 69)$. In addition, as pointed out in the previous subsection, some α_{xx} and α_{yy} are found to be higher than 100% meaning that the magnetic mode is located in a region where we have a concentration of the strain higher than the imposed one. Finally, we have used simple modeling by using equation 1 and by replacing $\sigma_{xx}^{sub}(\mathrm{V})$ by $\sigma_{xx}^{mode} = \alpha_{xx}\sigma_{xx}^{cf}(\mathrm{V})$ and $\sigma_{yy}^{sub}(\mathrm{V})$ by $\sigma_{yy}^{mode} = \alpha_{yy}\sigma_{yy}^{cf}(\mathrm{V})$ to try to fit the experimental data. The continuous lines in figure 6 are the corresponding fits. It is worth noting that we have made no supplementary fit than the one performed for the continuous film when determining λ. One can note good correlation between the modeling and the experimental data. This good correlation is partly due to the fact that the studied magnetic modes correspond to a static situation where the magnetization are almost uniform.

Conclusion

Differentiated strain control of magnetic modes have been performed in $Ni_{60}Fe_{40}$ antidot arrays by taking advantage of the specific features of magnetic antidot systems. This control has been possible due to the nanostructured character of the magnetic medium associated to the incorporation of a supporting compliant layer which allows the enhancement of the strain heterogeneity amplitude. This results in a very significant magneto-elastic field heterogeneity at the scale of the antidot primitive cell. Therefore, the localized magnetic modes are submitted to very different local fields as highlighted by *in situ* FMR measurements. Experimentally, we have taken advantage of the square-symmetry of the antidot arrays to study similar magnetic modes in two distinct strain maps. The experimental results agree well with the modeling involving micromagnetic simulations (to locate the magnetic modes), full-field simulations (to evaluate the strain field distributions) and an analytical model generally dedicated to a continuous film that we have extended to those magnetic modes.

Supporting informations

Nanofabrication of $Ni_{60}Fe_{40}$ antidot arrays

The IL principle involves the use of interference patterns generated from two obliquely incident beam paths to expose a photoresist layer as shown in figure 1-a) [46,47]. To this end, a 127.5 µm thick Kapton® layer was first spin coated with an Ultra-i 123 I-Line positive photoresist and then mounted on one arm of a Lloyd's-mirror Interferometer (see figure 1-a)) while the second arm of the interferometer holds a mirror. Both arms of the interferometer were exposed to a 325 nm continuous beam (He-Cd laser). The interference between the light from the source beam and the light reflected from the mirror form a standing wave pattern with alternating maxima and minima of intensity. Subsequently, a 90° rotation of the Kapton® layer is performed to allow a second exposure of the photoresist. After this double

exposure, the photoresist was developed in CD-26, then rinsed in DI water and dried using a nitrogen gun. In this condition, a dot pattern is obtained on top of the Kapton® layer. Then, a 20 nm $Ni_{60}Fe_{40}$film was deposited using the RF sputtering at a fixed Ar pressure of 3 mTorr. Lift-off of the deposited film was carried out in isopropyl alcohol (IPA). Completion of the lift-off process was determined by the color contrast of the patterned $Ni_{60}Fe_{40}$ area. The $Ni_{60}Fe_{40}$ material has been chosen because of its good ferromagnetic resonance (FMR) signal and for its non-zero magnetostriction.

Ferromagnetic measurements with *in situ* voltage-induced strains

Broadband ferromagnetic resonance (FMR) has been employed to detect spin waves with a zero wave vector in the antidot arrays and to study the influence of in-plane elastic strains on their energies by applying electrical voltage to the ferroelectric substrate. We remind here that this voltage induced magnetoelastic coupling is based on a two step process: first, the application of an electric field inside the ferroelectric substrate induces elastic strains to the antidot array *via* electromechanical effects[34] and secondly, magnetostriction of the magnetic antidots induces a magnetoelastic field which can be strain (or voltage)-tuned in amplitude and direction. In these conditions, a quantitative evaluation of this magnetoelastic coupling requires both the determination of the strains induced by the ferroelectric substrate to the magnetic antidots (or to the reference continuous film) through the Kapton® layer and the induced magnetoelastic field. This latter is directly measured *via* the FMR peak shifts for each detectable mode[45]. Concerning the strain inside the magnetic medium, it depends on whether one considers the antidot arrays or the reference continuous film. For this latter, the PZT substrate is perfectly calibrated so that macroscopic strains (ε_{xx}^{sub} and ε_{yy}^{sub}) in the substrate are known and are homogeneous across the whole top surface (15×7 mm^2). Moreover, previous works show that the macroscopic strains are fully transmitted through the thickness of the whole system[35,48]. The reasons are that the continuous thin film is much thinner than the Kapton® layer (about 3 and 4 orders of magnitude) and that

the interface is fully continuous. In the case of antidots, the mechanical problem is more complex. Indeed, the strain is heterogeneously distributed in the magnetic medium, because of nano-hole edges combined with the mechanical contrast between $Ni_{60}Fe_{40}$ and Kapton®, as it will be illustrated in the next section. Thus, we use full-field modeling to estimate quantitatively the strain distribution.

Numerical methods for magneto-mechanical behavior estimation

The micromagnetic simulations have been performed with the aim to locate the different magnetic modes and to calculate their frequency dependencies as a function of the applied magnetic field[26–29]. These latter dependencies can be directly compared to the FMR experiments. To this end, a square array of 16 antidots (diameter 250 nm with a periodicity of 600 nm) in a square cell with 2400 nm sides was created. Cuboid cells of volume $5 \times 5 \times 5$ nm^3 have been used. The parameters used in the simulations have been obtained from the FMR analysis of the continuous film (not shown here): $M_s = 950$ emu.cm^{-3}, $\frac{\gamma}{2\pi} = 0.0028$ GHz.Oe^{-1} and the exchange stiffness $A = 1.3 \times 10^{-6}$ erg.cm^{-1}. At a first step, the Landau-Lifshitz-Gilbert equation was solved with a damping constant fixed at $\alpha = 0.5$ for each system (CSA and SA) by applying a static magnetic field ranging from 100 to 2000 Oe by step of 50 Oe along $x-$axis allowing recording the equilibrium state. In a second step, the dynamic response of both systems is obtained by exciting the system with a short magnetic field pulse applied orthogonally which disturbs the equilibrium state. The system can thus relax following the LLG equation with a damping constant fixed at $\alpha = 0.008$. The magnetic pulse has the following form $\widetilde{h} = h_0 \mathrm{sinc}\left(2\pi f_{cut}(t - t_0)\right)$, where f_{cut} was fixed at 25 GHz with a sampling frequency $f_s = 200$ GHz giving a Nyquist frequency $f_n = 100$ GHz. Each dynamic simulation is calculated over 20 ns divided in 4000 stages and each stage is got by mean of the Runge Kutta algorithm. The Fourier transform method was used to get the resonance frequencies related to the different magnetic modes and their spatial localization. For this purpose, the magnetization configuration is stored for each elementary volume and

for each stage as well as the mean value of each component. Then, the Fourier transform of the magnetization component $m_y = \frac{M_y}{M_s}$ is calculated to obtain the resonance frequencies. The spacial absorption at the corresponding frequencies are then calculated using the averaged value of each elementary mesh cell over the thickness, since we consider the thickness small enough to get uniform distribution of the magnetization over it.

The strain field generated in the antidots induced by the PZT substrate is determined by finite element method within COMSOL Multiphysics®. The geometry of the systems consists of a Kapton® layer of dimensions $7.5 \times 7.5 \times 5$ μm^3 and a $Ni_{60}Fe_{40}$ magnetic antidot array of dimensions $7.5 \times 7.5 \times 0.02$ μm^3 containing 8×8 nanodots periodically distributed according to both SA and CSA systems. The interface between the polymer layer and the antidots is assumed to be perfect (perfect adhesion implying continuity of the displacement and the traction vector at the interface). It is worth noting that the represented thickness of the Kapton® layer (5 μm) is much lower than the real thickness (127.5 μm). This thickness is however sufficient to avoid possible perturbations that may be caused by the stiffer magnetic antidots on the average strain of the compliant layer. It is also worth noting that the PZT ferroelectric behavior is not modeled here, only the strain applied by the PZT to the Kapton® is modeled. All these justified modeling choices are motivated by optimization/reduction of the computing time. Thus, it is necessary during numerical simulations to replicate the homogeneous in-plane strains transmitted by the PZT substrate to the Kapton® layer. For this purpose, the following tensile-compression displacement loading will be applied to the Kapton® layer:

$$U_x = \epsilon_{xx}^{sub} x \quad / \quad x = \pm\frac{L}{2} \tag{3}$$

$$U_y = \varepsilon_{yy}^{sub} y \quad / \quad y = \pm\frac{L}{2} \tag{4}$$

U_x and U_y represent the displacement magnitudes applied quasi-statically to the Kapton® layer and L is the length of the Kapton® layer. Regarding the spatial discretization of

the calculation domain in accordance with the finite element method, the COMSOL Multiphysics automatic mesher was used. Special attention was paid to densify the mesh wherever necessary, i.e. in the neighborhoods of interfaces and free surfaces. An evolutive spatial discretization was thus carried out, utilizing a 1-degree tetrahedral Lagrangian finite element, with a minimum characteristic length of 10 nm. This length enables to have two rows of finite elements along the thickness of the deposit, which is sufficient to accurately calculate the mean strain in the antidots. Moreover, it has been checked that the adopted meshing density enables to reach the convergence of the numerical results. In view of the relatively small deformations involved here, the calculations are carried out within the linear framework of small perturbation assumptions. Within the small ranges of strain, the materials studied behave linearly in addition to being isotropic. Once the calculations are performed, a gage zone of dimensions 3×3 μm^2 was considered inside the antidot so as to avoid the disturbance induced by the free and loaded edges during the post-processing of the numerical results.

Acknowledgement

This work was supported by the French-Singaporean International Research Program (IRP CNRS-NUS Stretch-Smart) and in the frame of the ElecAcouSpin ANR project, grant ANR-19-CE24-0009 of the French Agence Nationale de la Recherche (ANR). In addition, ANR and CGI (Commissariat à l'Investissement d'Avenir) are gratefully acknowledged for their financial support through Labex SEAM (Science and Engineering for Advanced Materials and devices), ANR-10-LABX-0096 and ANR-18-IDEX-000. The authors want to thank Nicolas Greneche, responsible of the MAGI server in USPN for his support during the simulations.

References

(1) A. Fert, V. Cros and J. Sampaio, Skyrmions on the track, Nature Nanotechnology 8, 152 (2013)

(2) N. Nagaosa and Y. Tokura, Topological properties and dynamics of magnetic skyrmions, Nature Nanotechnology 8, 899 (2013)

(3) L. Liu, C.-F. Pai, Y. Li, H. W. Tseng, D. C. Ralph, R. A. Buhrman, Spin-Torque Switching with the Giant Spin Hall Effect of Tantalum, Science 336, 555 (2012)

(4) A. Kent, D. Worledge, A new spin on magnetic memories, Nature Nanotechnology 10, 187 (2015)

(5) R.E. Rottmayer et al., Heat-Assisted Magnetic Recording, IEEE Transactions on Magnetics 42, 2417 (2006)

(6) V. V. Kruglyak, S. O. Demokritov and D. Grundler, Magnonics ,J. Phys. D: Appl. Phys. 43 264001 (2010)

(7) J. Ding, M. Kostylev and A. O. Adeyeye, Magnonic Crystal as a Medium with Tunable Disorder on a Periodical Lattice, Phys. Rev. Lett. 107, 047205 (2011)

(8) A. Barman et al. J. Phys.: Condens. Matter, The 2021 Magnonics Roadmap, in press https://doi.org/10.1088/1361-648X/abec1a

(9) A. B. Ustinov, A. V. Drozdovskii, A. A. Nikitin et al., Dynamic electromagnonic crystal based on artificial multiferroic heterostructure,Communications Physics 2, 137 (2019)

(10) S. O. Sayedaghaee, B. Xu, S. Prosandeev C. Paillard and L. Bellaiche, Novel Dynamical Magnetoelectric Effects in Multiferroic BiFeO3, Phys. Rev. Lett. 122, 097601 (2019)

(11) A. K Biswas, J. Atulasimha and S. Bandyopadhyay, The straintronic spin-neuron, Nanotechnology 26, 285201 (2015)

(12) S. Mondal, Md A. Abeed, K. Dutta, A. De, S. Sahoo, A. Barman and S. Bandyopadhyay, Hybrid Magnetodynamical Modes in a Single Magnetostrictive Nanomagnet on a Piezoelectric Substrate Arising from Magnetoelastic Modulation of Precessional Dynamics,ACS Appl. Mater. Interfaces 10, 50, 43970 (2018)

(13) V. Garcia, M. Bibes and A. Barthélémy, Artificial multiferroic heterostructures for an electric control of magnetic propertiesHétérostructures multiferroïques artificielles pour un contrôle électrique des propriétés magnétiques, Comptes Rendus Physique 16, 168 (2015)

(14) C. A. F. Vaz, J. Hoffman, C. H. Ahn, and R. Ramesh, Magnetoelectric Coupling Effects in Multiferroic Complex Oxide Composite Structures, Advanced Materials 22, 2900 (2010)

(15) W. Eerenstein, N. D. Mathur and J. F. Scott, Multiferroic and magnetoelectric materials, Nature 442, 759 (2006)

(16) M. Buzzi et al., Single Domain Spin Manipulation by Electric Fields in Strain Coupled Artificial Multiferroic Nanostructures, Phys. Rev. Letters 111, 027204 (2013)

(17) Q. Wang, B. Heinz, R. Verba et al., Spin Pinning and Spin-Wave Dispersion in Nanoscopic Ferromagnetic Waveguides, Phys. Rev. Lett. 122, 247202 (2019)

(18) G. Gubbiotti, X. Zhou, Z. Haghshenasfard, M. G. Cottam, and A. O. Adeyeye, Reprogrammable magnonic band structure of layered permalloy/Cu/permalloy nanowires, Phys. Rev. B 97, 134428 (2018)

(19) Y. S. Gui, N. Mecking, and C.-M. Hu, Quantized Spin Excitations in a Ferromagnetic Microstrip from Microwave Photovoltage Measurements, Phys. Rev. Lett. 98, 217603 (2007)

(20) A. V. Chumak, V. I. Vasyuchka, A. A. Serga and B. Hillebrands, Magnon spintronics, Nature Physics 11, 453 (2015)

(21) A. V. Chumak, A. A. Serga and B. Hillebrands, Magnonic crystals for data processing, J. Phys. D: Appl. Phys. 50, 244001 (2017)

(22) B. W. Zingsem, T. Feggeler, A. Terwey, S. Ghaisari, D. Spoddig, D. Faivre, R. Meckenstock, M. Farle and M. Winklhofer, Biologically encoded magnonics, Nature Communications 10, 4345 (2019)

(23) Z. K. Wang, V. L. Zhang,H. S. Lim, S. C. Ng, M. H. Kuok, S. Jain and A. O. Adeyeye, Nanostructured magnonic crystals with size-tunable bandgaps, ACS Nano 4, 643 (2010)

(24) A. Casiraghi et al., Individual skyrmion manipulation by local magnetic field gradients, Communications Physics 2, 145 (2019)

(25) T.T. Nguyen, J. Yvonnet, Q.-Z. Zhu, M. Bornert and C. Chateau, A phase field method to simulate crack nucleation and propagation in strongly heterogeneous materials from direct imaging of their microstructure , Eng. Frac. Mechanics 139, 18 (2015)

(26) J. Ding, D. Tripathy and A. O. Adeyeye, Dynamic response of antidot nanostructures with alternating hole diameters, EPL, 98, 16004 (2012)

(27) G. Gubbiotti, F. Montoncello, S. Tacchi, M. Madami, G. Carlotti, L. Giovannini, J. Ding and A. O. Adeyeye, Angle-resolved spin wave band diagrams of square antidot lattices studied by Brillouin light scattering, Appl. Phys. Lett. 106, 262406 (2015)

(28) S. Neusser, B. Botters, M. Becherer, D. Schmitt-Landsiedel and D. Grundler, Spin-wave localization between nearest and next-nearest neighboring holes in an antidot lattice, Appl. Phys. Lett. 93, 122501 (2008)

(29) R. Mandal, S. Saha, D. Kumar, S. Barman, S. Pal, K. Das, A. Kumar Raychaudhuri, Y. Fukuma, Y. Otani and A. Barman, Optically Induced Tunable Magnetization Dynamics in Nanoscale Co Antidot Lattices, ACS Nano, 6, 4, 3397 (2012)

(30) N. Challab, F. Zighem, D. Faurie, M. Haboussi, M. Belmeguenai, P. Lupo and A. O. Adeyeye, Local Stiffness Effect on Ferromagnetic Response of Nanostructure Arrays in Stretchable Systems, Phys. Status Solidi RRL 13, 1800509 (2019)

(31) M. Gueye, F. Zighem, D. Faurie, M. Belmeguenai and Silvana Mercone, Optimization of indirect magnetoelectric effect in thin-film/substrate/piezoelectric-actuator heterostructure using polymer substrate, Appl. Phys. Lett. 105, 052411 (2014)

(32) M. Donahue, and D. G. Porter, OOMMF User's Guide, Version 1.0, Intergency Report NISTIR 6376 (National Institute of Standard and Technology, Gaithersburg, MD). http://math.nist.gov/oommf

(33) COMSOL Multiphysics® v. 4.4, www.comsol.com. COMSOL AB, Stockholm, Sweden

(34) T. Sadat, D. Faurie, P. Godard, D. Thiaudière, P.-O. Renault and F. Zighem, 90° ferroelectric domain switching effect on interfacial strain mediated magnetoelectric coupling, J. Phys. D: Appl. Phys. 53, 145001 (2020)

(35) F. Zighem, M. Belmeguenai, D. Faurie, H. Haddadi, and J. Moulin, Combining ferromagnetic resonator and digital image correlation to study the strain induced resonance tunability in magnetoelectric heterostructures, Rev. Sci. Inst. 85, 103905 (2014)

(36) M. Bailleul, R. Höllinger, and C. Fermon, Microwave spectrum of square Permalloy dots: Quasisaturated state, Phys. Rev. B 73, 104424 (2006)

(37) C. Bayer, S. O. Demokritov, and B. Hillebrands and A. N. Slavin, Spin-wave wells with multiple states created in small magnetic elements, Appl. Phys. Lett. 82, 607 (2003)

(38) S. Neusser, B. Botters and D. Grundler, Localization, confinement, and field-controlled propagation of spin waves in Ni80Fe20 antidot lattices, Phys. Rev. B 78, 054406 (2008)

(39) R. D. McMichael and B. B. Maranville, Edge saturation fields and dynamic edge modes in ideal and nonideal magnetic film edges, Phys. Rev. B 74, 024424 (2006)

(40) B. B. Maranville, R. D. McMichael, S. A. Kim, W. L. Johnson, C. A. Ross and J. Y. Cheng, Characterization of magnetic properties at edges by edge-mode dynamics, J. Appl.. Phys. 99, 08C703 (2006)

(41) F. Zighem, Y. Roussigné, S.M. Chérif and P. Moch, Spin wave modelling in arrays of ferromagnetic thin stripes: application to Brillouin light scattering in permalloy, J. Phys.: Condens. Matter 19, 176220 (2007)

(42) G Gubbiotti, M Kostylev, S. Tacchi, M. Madami, G. Carlotti, J. Ding, A. O. Adeyeye, F. Zighem, A. A. Stashkevich, E. Ivanov and S Samarin, Collective spin waves on a nanowire array with step-modulated thickness, J. Phys. D: Appl. Phys. 47, 105003 (2014)

(43) P. Djemia, C. Dugautier, T. Chauveau, E. Dogheche, M. I. De Barros, L. Vandenbulcke, Mechanical properties of diamond films: A comparative study of polycrystalline and smooth fine-grained diamonds by Brillouin light scattering, J. Appl. Phys., 90, 3771 (2001)

(44) M. Gueye, F. Zighem, M. Belmeguenai, M. Gabor, C. Tiusan and D. Faurie, Ferromagnetic resonance in thin films submitted to multiaxial stress state: application of the uniaxial equivalent stress concept and experimental validation, J. Phys. D: Appl. Phys. 49 265001 (2016)

(45) F. Zighem, D. Faurie, S. Mercone, M. Belmeguenai and H. Haddadi, Voltage-induced strain control of the magnetic anisotropy in a Ni thin film on flexible substrate, J. Appl. Phys. 114, 073902 (2013)

(46) F. Zighem, D. Faurie, M. Belmeguenai, A. Garcia-Sanchez, P. Lupo, and A. O. Adeyeye, Large area periodic ferromagnetic nanowires deposited onto a polymer substrate, Appl. Phys. Lett. 111, 052408 (2017)

(47) C. Lu and R. H. Lipson, Interference lithography: a powerful tool for fabricating periodic structures, Laser Photonics Rev. 4, 568 (2010)

(48) F. Zighem, A. El Bahoui, J. Moulin, D. Faurie, M. Belmeguenai, S. Mercone and H. Haddadi, Micro-strip ferromagnetic resonance study of strain-induced anisotropy in amorphous FeCuNbSiB film on flexible substrate, J. Appl. Phys. 116, 123903 (2014)